Highly Entangled Magnetodielectric and Magnetostriction effects, and Spin-Phonon coupling in the Antiferromagnetic Ni₂ScSbO₆

Neha Patel¹, Arkadeb Pal^{2,3†}, C. W. Wang⁴, G. R. Blake³, J. Khatua⁵, T. W. Yen², Susaiammal Arokiasamv⁶, H. S.

Kunwar⁷, Y. C. Lai⁴, Y. C. Chuang⁴, V. Sathe⁷, Kwang-Yong Choi⁵, H. D. Yang², Sandip Chatterjee^{1*}

¹Department of Physics, Indian Institute of Technology (BHU) Varanasi, 221005, India

²Department of Physics, National Sun Yat-sen University, Kaohsiung 80424, Taiwan

³Zernike Institute for Advanced Materials, University of Groningen, 9747 AG Groningen, The Netherlands

⁴National Synchrotron Radiation Research Center, Hsinchu, 30076, Taiwan

⁵Department of Physics, Sungkyunkwan University, Suwon 16419, Republic of Korea

⁶Department of Physics, St. Bede's College, Navbahar, Shimla 171002, India

 7UGC -DAE Consortium for Scientific Research, University Campus, Khandwa Road, Indore 452001, India

Corresponding authors: †pal.arkadeb@gmail.com; *schaterji.app@iitbhu.ac.in

ABSTRACT

Magnetic systems with noncentrosymmetric crystal structures are renowned for their complex magnetic ordering and

diverse and fascinating physical properties. In this report, we provide a comprehensive study of the chiral magnetic

system Ni₂ScSbO₆, which exhibits a robust incommensurate long-range antiferromagnetic spin ordering at a

temperature of $T_N = 62$ K, as revealed by bulk magnetization, specific heat, and neutron diffraction studies. This

magnetic ordering triggers a series of intriguing phenomena, including prominent magnetodielectric coupling

manifested by a dielectric peak at T_N , significant spin-phonon coupling resulting in strong phonon renormalization

characterized by anomalous softening of various Raman modes, and a remarkable volume magnetostriction effect

probed by high-resolution synchrotron X-ray diffraction. These phenomena are intricately interlinked, positioning

the present system as a rare and interesting material.

INTRODUCTION

The quest for advanced, energy-efficient spintronics devices has sparked a surge in investigations focused on multifunctional materials that exhibit a diverse array of mutually entangled properties. The close correspondence among various microscopic degrees of freedom in these systems - such as spin, orbital, charge, lattice, dipole, and phonon–lays the groundwork for controlling one property through the conjugate field of another [1–4]. In this context, magnetoelectric and magnetodielectric (MD) materials have garnered substantial attention for their potential to realize practical applications, such as tunable filters, magnetic sensors, and spin-charge transducers [5–8]. While both intrinsic and extrinsic mechanisms (such as the Maxwell–Wagner effect) have been proposed to explain the origin of the MD effect, intrinsic mechanisms hold promise for envisioning devices with faster switching and reduced losses. Apart from such technological prospects, investigating MD properties across various classes of magnets also contributes to our understanding of coupled properties that stem from the inherent antagonism between spin and dipolar origins. The exploration of systems with complex magnetic ordering can be an efficacious means towards crafting novel MD and/or magnetoelectric materials.

On the other hand, fascinating effects emerge from the excitations of collective modes in condensed matter, such as spin waves, and phonons coupled with spin ordering, which constitute a fundamental facet of lattices that contain magnetic ions. These phenomena, predominantly governed by magnetic exchange interactions, occur when such materials are exposed to electromagnetic waves [9]. To address the modern need for device miniaturization, such properties offer a promising path for integrated low-power computation and signal processing, owing to their lack of Joule loss. Moreover, the strong entanglement of spin-lattice-phonon degrees of freedom may trigger further intriguing phenomena such as superconductivity, the phonon Hall effect, spin-Seebeck effect, spin-Peierls transitions, magnetoelectric or MD coupling, and the giant thermal Hall effect [10–16].

Insulating systems with a noncentrosymmetric crystal structure and complex spin ordering can host intriguing effects, including multiferroicity, solitons, skyrmions, the linear electro-optic effect, and the piezoelectric effect [17–24]. These magnetic systems have attracted significant attention in the emerging fields of terahertz and sub-terahertz magnonics and antiferromagnetic spintronics. In this context, the AFM magnet Ni₂ScSbO₆, part of the chiral corundum structured family related to Ni₃TeO₆, is of particular interest. Recent research has focused on compounds derived from Ni₃TeO₆, such as Ni₂InSbO₆, Mn₂MnWO₆, Mn₂InSbO₆, and Co₂InSbO₆ [25–29]. Despite their similar crystal structures and symmetry, these compounds exhibit distinct spin orderings and varied physical properties. Ivanov *et al.* first synthesized and investigated the compounds Ni₂ScSbO₆ and Ni₂InSbO₆ for their crystal

and spin structures in 2013. Unlike the commensurate collinear AFM order observed in Ni₃TeO₆, both Ni₂ScSbO₆ and Ni₂InSbO₆ were reported to exhibit antiferromagnetically coupled incommensurate helices [30]. Subsequently, Ni₂InSbO₆ has been studied extensively by various groups, particularly for its intriguing magnetic and multiferroic properties [26]. On the contrary, despite having similar crystal structure, research on Ni₂ScSbO₆ has remained limited, with many of its properties largely unexplored. In this report, we present a comprehensive study of the crystal and spin structures, magnetization, dielectric, magnetodielectric, and lattice dynamics properties of Ni₂ScSbO₆.

II. EXPERIMENTAL METHODS

A polycrystalline sample of Ni₂ScSbO₆ was prepared using the conventional solid-state reaction route. For the reactions, dried high-purity oxide powders of NiO, Sc₂O₃, and Sb₂O₅, with purities exceeding 99.99% (Alfa-Aesar), were mixed as precursors in the appropriate stoichiometric ratio. The mixture was intimately ground for several hours and then formed into pellets. The resulting pellets were initially sintered at 700°C for 24 hours, then ground into fine powder, pressed, and annealed multiple times at temperature intervals of 100°C up to 1200°C. The series of grinding and sintering was repeated until the X-ray diffraction (XRD) pattern exhibited no impurity peaks. Finally, the samples were sintered at 1300°C for 48 hours. The resulting product was greenish yellow in color, which was assessed for phase purity by performing a synchrotron X-ray diffraction (SXRD) measurement at T = 300 K at the Taiwan Photon Source (TPS) 19A beamline of the National Synchrotron Radiation Research Center (NSRRC), Taiwan, using X-rays with a wavelength (λ_i) of 0.77489 Å. Additionally, T-dependent SXRD patterns were collected over the range of 300–20 K. Two setups with different wavelengths were used in two distinct temperature regimes: $\lambda_i = 0.77489$ Å for T = 300-100 K and $\lambda_i = 0.61992$ Å for T = 100-20 K. Magnetization measurements were conducted using a commercial SQUID-based magnetometer (MPMS, Quantum Design). Various dielectric measurements were conducted utilizing a precision Agilent E4980A LCR meter coupled with a custom dielectric probe within a Quantum Design MPMS, facilitating control over both magnetic field (H) and temperature (T). Specific heat measurements (C_P) were carried out utilizing a heat-pulsed thermal relaxation calorimeter within a Quantum Design physical property measurement system (PPMS). Raman data were collected using a Horiba Jobin Yvon HR-800 spectrometer equipped with an 1800 g/mm grating, an edge filter for Rayleigh line rejection, and a CCD detector. A 473 nm diode laser served as the excitation source in a backscattering geometry for the Raman measurements. Thermal control was maintained with a Janis ST-500 continuous helium flow cryostat, ensuring a thermal stability of ± 0.1 K.

III. RESULTS AND DISCUSSIONS

A. Crystal structure

The high-resolution SXRD pattern of Ni₂ScSbO₆ acquired at T = 300 K, along with its fitted Rietveld profile, is illustrated in Fig. 1(a). The refinement indicates a single-phase trigonal structure with chiral symmetry R3, consistent with prior studies. No impurities were discerned. Detailed crystallographic data, including lattice parameters and Wyckoff positions, are provided in Table SI of the supplemental material (SM) [31], which are congruent with previously reported values [30]. The crystal structure of Ni₂ScSbO₆ is illustrated in Figs. 1(b)–(d), depicting interconnected networks of NiO₆, ScO₆, and SbO₆ octahedra. Ni atoms, occupying distinct crystallographic sites Ni(1) and Ni(3), are situated on consecutive layers within the ab plane, separated by a distance of 0.1667 c. Additionally, Sc and Sb atoms reside on the same planes as Ni(3) and Ni(1), respectively. Thus, the structure comprises two-dimensional (2D) honeycomb layers on the ab planes, composed of alternately spaced edge-shared Ni(1)O₆ (or Ni(3)O₆) and SbO₆ (or ScO₆) octahedra, as shown in Fig. 1(c). Notably, when examining the nearest neighbor magnetic atoms on the ab planes, both Ni(1) and Ni(3) form triangular networks within their respective ab planes, as depicted in Fig. 1(c). This triangular lattice arrangement of Ni atoms becomes particularly evident when observing a specific ab plane, as demonstrated in Fig. 1(d).

B. Magnetization

The temperature dependence of the DC magnetization (M) measured using zero-field cooled (ZFC) and field cooled (FC) protocols under an applied field of H = 0.05 T is presented in Fig. 2(a). The M(T) curves exhibit a sharp λ -like transition at $T_N = 62$ K, which indicates long-range AFM ordering. The observed T_N is close to, but slightly higher than, the previously reported value (~ 60 K) for this system [30]. At temperatures below 30 K, M slightly increases as T decreases, likely due to the presence of defects or orphan spins that behave like paramagnetic spins, a phenomenon commonly observed in other AFM systems [32,33]. The inverse susceptibility ($1/\chi$) versus T data for H = 2 T was fitted in the paramagnetic region (T = 120 K - 300 K) using the modified Curie-Weiss (CW) law, expressed as: $\chi = \chi_0 + \frac{c}{(T - \theta_{CW})}$ [34]. Here, χ_0 is the T-independent susceptibility incorporating two distinct terms: the core diamagnetism arising from the core-electron shells (χ_{core}) of all the constituent atoms and the openshell Van Vleck paramagnetism (χ_{VV}) associated with Ni²⁺. C represents the Curie constant, and θ_{CW} refers to the characteristic CW temperature. The fit is displayed in the inset of Fig. 2(a) and yielded $\chi_0 = -9.563 \times 10^{-4}$ emu/(mole-Oe), an effective paramagnetic moment (μ_{eff}) of 2.94 μ_B/Ni^{2+} , and $\theta_{CW} = -87$ K. The large negative value of θ_{CW}

indicates that AFM interactions are dominant. The experimentally obtained value of μ_{eff} closely matches the theoretical spin-only moment (μ_{theor}) of 2.82 $\mu_{\rm B}$ expected for Ni²⁺ ions. This is in agreement with X-ray absorption spectroscopy (XAS) data at the Ni $L_{2,3}$ edge (see Fig. S2 of SM). Furthermore, an isothermal M(H) curve was recorded at T=2 K, as shown in Fig. 2(b). The linear, non-saturating, and non-hysteretic behavior of the curve clearly suggests that the system possesses overall AFM character.

C. Specific heat

The T-dependence of the zero-field specific heat (C_p) is shown in Fig. 2(c), which exhibits a λ -like anomaly at $T_N = 62$ K, thus suggesting the development of a long-range ordered (LRO) magnetic state. This observation aligns with the magnetization and neutron powder diffraction (NPD) studies (discussed below) on this system. In insulating magnets, the C_p predominantly originates from phonon excitations at high temperatures, while at low temperatures, it is mainly influenced by magnetic interactions. Thus, to determine the magnetic specific heat (C_{mag}) , the phononic component ($C_{lattice}$) was subtracted from the overall C_p . $C_{lattice}$ was estimated by fitting our $C_p(T)$ data in the high-Trange (T = 80 - 200 K) and then extrapolating down to 2 K, as depicted by the red line in Fig. 2(c). This fitting was performed using the Debye model (with two Debye functions) [35], expressed as : $C_{lattice}(T)$ = $9k_B \left[\sum_{n=1}^2 C_n \left(\frac{T}{\theta_{D_n}} \right)^3 \int_0^{\theta_{D_n}/T} \frac{x^4 e^x}{(e^x - 1)^2} dx \right]$, where k_B refers to the Boltzmann constant, θ_{D_n} (n = 1, 2) denotes the characteristic Debye temperatures, and C_n represents the integer coefficients. The best fit, which satisfactorily reproduces the experimentally recorded $C_p(T)$ data at high temperatures, yielded $\theta_{D_1} = 290$ K and $\theta_{D_2} = 920$ K. The coefficients C_1 and C_2 were fixed at a ratio of 1:1.5, representing the ratio of the total number of heavier metal atoms to the total number of lighter oxygen atoms. The resulting C_{mag}/T curve as a function of T is shown in Fig. 2(d). Besides the sharp peak at T_N , a broad feature is observed near $T \sim 30$ K, possibly associated with the reentrant glassy state indicated by the ac-susceptibility study (Fig. S1 of SM), which may originate from spin frustration and minor lattice defects or disorders. Similar, broad shoulder-like features have previously been reported for other spinfrustrated systems [36]. The magnetic entropy (S_{mag}) was estimated by integrating the C_{mag}/T curve, as shown in Fig. 2(d). Approximately 78% of the total S_{mag} is released at T_N , and the remainder is recovered above T_N . Above T=80K, S_{mag} reaches a saturation value of ~9.08 J/mol-K, which matches well with the theoretically expected magnetic entropy ~ 9.13 J/mol-K for Ni²⁺ spins (S = 1). This observation is consistent with the $1/\chi$ vs. T curve, which demonstrates a deviation from Curie-Weiss behavior below $T \approx 80$ K (inset of Fig. 2(a)), typical for the presence of short-range magnetic ordering above T_N [34,37]. $C_p(T)$ data were also collected under various applied H up to 7 T,

as shown in the inset of Fig. 2(c). The peak associated with T_N is substantially suppressed and shifted towards lower temperature with increasing H, which are typical characteristics of AFM systems.

D. Neutron Powder Diffraction

NPD was performed on Ni₂ScSbO₆ under zero-field and applied magnetic fields up to 4 T to gain insight into its spin ordering. As the temperature drops below 60 K, magnetic Bragg peaks appear, with some existing nuclear peaks gaining intensity and two new magnetic reflections emerging. This is evident in the NPD patterns at T = 2 K and 50 K (Fig. 3(a)), where a new pair of magnetic peaks forms on either side of the nuclear peak at 32°. This appears as broadening compared to the nuclear reflections observed at a temperature higher than T_N, i.e., 70 K, shown in Fig. 3 (a). To isolate the signal associated with magnetic ordering, the 70 K NPD data were subtracted from the 2 K and 50 K data, as depicted in Fig. 3 (b). The newly emerged magnetic peaks could not be indexed to the fundamental unit cell of the nuclear structure, indicating the presence of an incommensurate magnetically modulated spin structure. The NPD data collected at T = 2 K were analyzed using several candidate incommensurate magnetic models, including amplitude-modulated and orientation-modulated spin structures. Four models exhibited reasonably good fits, as summarized in Table I. The corresponding fitted data are shown in Fig. 3(c) for model 1 and in Fig. S4 [(a) to (c)] of the SM for models 2 to 4, respectively. The spin modulation, characterized by a propagation vector k = (0, 0.03575, 0) relative to the trigonal nuclear unit cell, was obtained from these fittings. As evident from Table I, models 1 to 3 yielded similar goodness-of-fit values, with the best fit achieved for a sinusoidal spin-density wave (SDW). The average refined moment for the SDW model fit is $2.7261 \times 2/\pi = 1.735 \,\mu_B/\mathrm{Ni}^{2+}$ at 2 K, which is close to the theoretically expected moment of 2 μ_B for S=1. The slightly reduced moment value can be attributed to strong quantum fluctuations that prevent the spins from achieving full order, a phenomenon also reported in other systems [38]. In contrast, model 4 exhibited considerably poorer fitting parameters compared to the other three models; thus, it can be ruled out as a possible spin structure for Ni₂ScSbO₆. A relatively close values of the goodness-of-fit parameters for the models 1 to 3 indicate that we cannot definitively assert the SDW model as the only viable option, despite its superior fitting parameters. Alternate models 2 and 3, including the helical spin ordering (i.e., model 2) proposed in a previous report [39], may also represent feasible spin configurations in Ni_2ScSbO_6 . In fact, a similar helical spin structure with slightly different k vectors: k = [0, 0.036(1), 0] for Ni_2ScSbO_6 and k = [0, 0.029(1), 0], was suggested in the previous study [39]. However, it is important to note that Ni₂InSbO₆ has been reported to exhibit a pronounced ferroelectric polarization below its T_N and multiferroic behavior, which can be attributed to a magnetostriction effect and its inherent helical spin structure [3,39,40]. In contrast, our current study showed that Ni₂ScSbO₆ lack any trace of ferroelectric polarization (to be discussed later), thus it is not a multiferroic candidate, unlike Ni₂InSbO₆. This fundamental distinction suggests that the spin structure of Ni₂ScSbO₆ is essentially different from that of Ni₂InSbO₆. Notably, a sinusoidal SDW spin ordering does not allow for ferroelectric polarization, thus ruling out multiferroicity [41]. In this context, it is plausible to attribute the absence of multiferroicity in Ni₂ScSbO₆ to the sinusoidal SDW spin ordering, as suggested by our NPD data analysis. However, further investigations using single-crystal neutron diffraction may be beneficial for obtaining a clearer understanding of the spin structure in this system.

During the phase transition from the paramagnetic to an ordered state (viz., AFM) at T_N , the intensity of the 003 magnetic Bragg peak can be described by the equation $I(T) = I_{PM} + [I_0(1 - T/T_N)^{2\beta}]$. The first term represents the intensity variation in the paramagnetic region ($T > T_N$), while the second term corresponds to the AFM region ($T < T_N$). Here, I_0 is the intensity as T approaches 0 K, and the critical exponent β characterizes the nature of the magnetic ordering. Generally, during a phase transition at $T = T_N$, the magnetic order parameter $m \propto \sqrt{I}$. The fitted temperature-dependent integrated intensity of the magnetic reflection (0 0 3) is plotted in Fig. 3 (d). This fit yielded $T_N = 60.6973(4)$ K and a critical exponent $\beta = 0.2198(5)$. The value of T_N is consistent with our bulk magnetization and specific heat measurements. Magnetic systems, depending on their spatial dimensionality and spin characteristics, fall into distinct categories with characteristic β values, such as $\beta = 0.125$ for the 2D Ising model, $\beta = 0.33$ for the 3D Ising model, $\beta = 0.35$ for the 3D XY model, and $\beta = 0.36$ for the 3D Heisenberg model. The β value of 0.2198(5) for Ni₂ScSbO₆ falls within an intermediate regime between the 2D and 3D Ising models. Furthermore, to examine the influence of an external magnetic field on the magnetic ordering, we recorded NPD patterns under magnetic fields up to 4 T at T = 2 K. The zero-field NPD data were subtracted from those collected at 4 T, as shown in Fig. S3 (a) of SM. No significant changes indicative of an altered spin structure were observed, demonstrating the robustness of the spin structure under applied magnetic fields, at least up to 4 T.

E. Dielectric and Magnetodielectric properties

The combination of a polar crystal structure and complex spin ordering in Ni₂ScSbO₆ implies potentially interesting dielectric and MD properties. The isostructural compound Ni₂InSbO₆ has been reported to exhibit a spin-driven ferroelectric phase transition at its $T_N = 76$ K [26], but these properties are still unexplored in Ni₂ScSbO₆. The dielectric constant (ε') is plotted as a function of temperature under H = 0 T for various frequencies (f) in Fig. 4(a). The $\varepsilon'(T)$ curves exhibit a λ -shaped peak at $T_E = T_N = 62$ K. The peak position is f-independent, whereas the value of ε' increases over the entire temperature range of interest with increasing f; the dielectric loss (tan δ) is negligibly small (\sim 0.0001-0.0003), a characteristic typical of highly insulating materials. These observations imply

that extrinsic contributions to ε' and dielectric relaxation behavior can be ruled out. To investigate whether the peak in $\varepsilon'(T)$ is associated with a ferroelectric phase transition, pyrocurrent (I_p) measurements were conducted both with and without the application of magnetic field. Despite examining multiple samples, no significant I_p signal was detected. Our SXRD study (see below) reveals a significant magnetostriction effect that is likely associated with the $\varepsilon'(T)$ peak. Although magnetostriction can induce ferroelectric polarization (P) in various systems, leading to multiferroicity [27,42], the absence of an I_p signal in Ni₂ScSbO₆ apparently suggests a distinctly different nature to the isostructural compound Ni₂InSbO₆.

To investigate whether Ni₂ScSbO₆ exhibits MD coupling, $\varepsilon'(T)$ curves were measured under the application of various magnetic fields, as shown in Fig. 4(b). The $\varepsilon'(T)$ peak is suppressed significantly with increasing H. Moreover, the peak shifts towards lower T, which can be ascribed to the typical suppression of T_N with field for AFM systems. According to the Lyddane-Sachs-Teller (LST) relation, the dielectric permittivity can be inherently coupled to the optical phonons, which can be expressed as $\frac{\varepsilon_0}{\varepsilon_\infty} = \prod_j \frac{\omega_{LOj}^2}{\omega_{TOj}^2}$; here ε_0 refers to the static dielectric constant, ε_{∞} represents the optical dielectric constant, ω_{LO} and ω_{TO} denote the long-wavelength longitudinal (LO) and transverse (TO) optical-phonon mode frequencies, respectively [34,43]. Generally, ω_{LO} is a T-independent parameter, whereas ω_{TO} is closely linked to the $\varepsilon'(T)$ curves. According to the modified Barrett theory, this relation is expressed as $\varepsilon'(T) = \varepsilon'(0) + A/[\exp(\frac{\hbar\omega_0}{k_BT}) - 1]$, where A denotes a coupling constant and ω_0 represents the average frequency of the low-lying phonon modes [43]. The $\varepsilon'(T)$ curves of Ni₂ScSbO₆ closely follow the Barrett theory above T_N , as shown in the inset of Fig. 4(b). However, $\varepsilon'(T)$ deviates from the Barrett curve near T_N , thereby indicating MD coupling. The fit parameters obtained are $\varepsilon'(0) = 7.283$, A = 0.531 and $\omega_{\theta} = 291.38$ cm⁻¹. The obtained value of ω_0 is consistent with the observed low-lying Raman mode frequencies (see below). A similar scenario has been observed in other systems exhibiting the MD effect, which has been attributed to the magnetostriction effect combined with spin-phonon coupling (SPC) [14,42,44]. Ni₂ScSbO₆ exhibits a pronounced SPC effect (to be discussed later) below T_N , which may be a plausible origin for the MD coupling in this system.

The isothermal dependence of ε' at T=2 K is shown in Fig. 4 (c). With increasing H, a distinct and systematic decrease in ε' is observed. The associated MD coupling parameter $(MD\%) = [\varepsilon'(0) - \varepsilon'(H)/\varepsilon'(0)] \times 100\%$ was calculated, and is shown in the inset of Fig. 4 (c). This further confirms the occurrence of a pronounced MD coupling in this system.

F. Temperature-dependent Raman spectroscopy: Spin-phonon coupling

Raman spectroscopy stands out for its unique ability to pinpoint structural alterations or distortions on a local scale, alongside gauging electronic excitations, the degree of cationic ordering, and SPC in various systems. In the case of Ni₂ScSbO₆, the potential existence of SPC was hinted at by the deviation of $\varepsilon'(T)$ from the LST relation near T_N , as described above. Therefore, to seek direct evidence of SPC and explore the phonon behavior in Ni₂ScSbO₆, especially around $T_N = 62$ K, a temperature-dependent Raman spectroscopy study was conducted, as illustrated in Figs. 5 (a)-(c). The spectra show no signals of structural phase transitions within the studied temperature range, as the mode distribution remains consistent down to 10 K, aligning with SXRD results discussed below. This aligns with the results obtained from SXRD (discussed below). However, a relatively broad peak centered at $\omega = 159$ cm⁻ ¹ emerges below 150 K. In the absence of any structural phase transitions within this temperature range, the peak may be associated with a magnon (M) mode, which is often observed at temperatures well above the long-range magnetic ordering temperatures [45–48]. Moreover, a relatively large blueshift ($\Delta\omega \sim 6$ cm⁻¹) of the suspected magnon peak in Ni₂ScSbO₆ is observed as T is decreased from 150 to 10 K, as shown in the SM, Fig. S6. A similar large blueshift was reported for a magnon peak pertaining to the AFM system FePS₃ [49]. The temperature variation (T-variation) of the linewidth (T) of this possible magnon mode (M) closely follows T^{α} behavior below T_N , where α ≈ 4.06 (inset of SM Fig S6) [31]. In fact, the linewidth of a magnon mode within a small T-regime is predicted to follow T 4 behavior according to the Hartree-Fock approximation [50]. To confirm the magnon mode unambiguously, further investigation of this peak under a magnetic field may be beneficial.

Utilizing a group theory-based symmetry analysis on the Ni₂ScSbO₆ structure, characterized by trigonal symmetry R3 (no. 146) with a point group C_3 (3), predicts a total of 30 possible modes at the Γ -point of the Brillouin zone. The phonons exhibiting infrared (IR) and Raman responses are predicted to consist of 27 simultaneously active Raman (9 A + 9 ${}^{1}E$ + 9 ${}^{2}E$) and IR (9 A + 9 ${}^{1}E$ + 9 ${}^{2}E$) modes, along with three acoustic modes (A + ${}^{1}E$ + ${}^{2}E$). Here, the symmetry E corresponds to a doubly degenerate mode. The Raman peaks observed are labeled as P1-P23 in Fig. 5, and detailed information regarding the tentative symmetry assignments is summarized in Table SII of the SM [31].

In general, for a magnetic system, the *T*-variation of a phonon mode frequency ω is described as: $\omega(T) = \omega_0 + \Delta\omega_{latt}(T) + \Delta\omega_{anh}(T) + \Delta\omega_{e^-ph}(T) + \Delta\omega_{s^-ph}(T)$, where ω_0 represents the frequency at an initial temperature T_0 , $\Delta\omega_{latt}$ arises from the contraction or expansion of the crystal lattice, $\Delta\omega_{anh}$ stands for the anharmonic contribution, and $\Delta\omega_{e^-ph}$ and $\Delta\omega_{s^-ph}$ represent the changes originating from electron-phonon and spin-phonon couplings, respectively. Ni₂ScSbO₆ is highly insulating in nature, thus any contribution from $\Delta\omega_{e^-ph}$ can be neglected. Our analysis shows

that the integrated peak intensities (I_R) of various Raman peaks exhibit anomalies at T_N , thus signaling a possible correlation between spins and phonons in this system as shown in SM. In the absence of spin-phonon coupling and any structural changes or lattice distortions, the temperature dependence of ω can be described solely by the anharmonic behavior outlined in Balkanski's model: $\omega_{anh}(T) = \omega_0 - C\left(1 + \frac{2}{\frac{\hbar\omega_0}{2k_BT}}\right)$; here, C is a variable parameter, \hbar denotes the reduced Planck's constant, and k_B signifies the Boltzmann constant [51]. Thus, a phonon mode exhibiting anharmonic behavior is anticipated to exhibit a low-T plateau in frequency, succeeded by a linear decrease at elevated temperatures. The Raman modes of Ni₂ScSbO₆ with high or moderate intensities were analyzed using Lorentzian spectral decomposition. Anharmonic fitting was performed on these curves (shown in red) in the elevated T region (T > 60 K). Notably, its several modes deviate from the expected anharmonic behavior, as shown in SM, Fig. S8. Figure 5(c) depicts the $\omega(T)$ curve for the P10 mode with the maximum deviation. The pronounced degree of anomalous softening observed below T_N is a typical signature of SPC [1,14,42,52–54]. For some modes, the deviation of $\omega(T)$ from the anharmonic model begins above T_N , which is attributable to significant short-range magnetic ordering, as evidenced by our magnetization and specific heat studies. In the magnetically ordered state of a system, the development of strong spin correlations can cause phonon renormalization, which can be described by a formalism proposed by Granado et. al. According to this formalism, [55] the relation between the nearest-neighbor spin-spin correlation function $\langle S_i, S_j \rangle$ and the change in the phonon frequency $(\Delta \omega_{s-ph})$ can be expressed as: $\Delta\omega_{s-ph}(T) \approx \lambda \langle S_i, S_j \rangle \approx \lambda \left\{ \frac{M(T)}{M_{Max}} \right\}^2$; wherein λ is a constant measuring the strength of the SPC and $M(T)/M_{Max}$ refers to the T variation of the normalized M curve with respect to maximum value of M, i.e. M_{Max} . Plots of $\Delta \omega$ and $\left\{\frac{M}{M_{Max}}\right\}^2$ versus T are shown for modes P10 and P22 in Figs. 7 (a), (b), which display matching trends from T_N down to T = 30 K. A similar result is found for the other modes with anomalous phonon softening, as shown in Fig. S9 of the SM [31]. This clearly confirms the presence of SPC. It is relevant here to mention that a frequency-dependent peak in the ac susceptibility $[\chi''(T)]$ data was observed near T = 30 K, which is likely attributed to a reentrant glassy state associated with the partial freezing of spins in this temperature range (see Fig. S1 in the SM) [34]. This is possibly the reason why the phonon renormalization does not follow $\left\{\frac{M}{M_{Max}}\right\}^2$ behavior at lower temperatures. Similar to $\omega(T)$, the corresponding $\Gamma(T)$ curves can be described by an anharmonic relation expressed as follows: $\Gamma_{anh}(T) = 0$ $\Gamma_0 + A\left(1 + \frac{2}{\frac{\hbar\omega_0}{2Kr^T}}\right)$; here A is an adjustable parameter, and Γ_0 represents Γ as $T \to 0$ K [42,51]. The $\Gamma(T)$ curves of P10 and P22 Raman modes, along with their anharmonic fits (shown in red), are presented in the insets of Figs. 6

(a) and (b), respectively. The $\Gamma(T)$ curves for the other analyzed modes are shown in Fig. S10 of the SM [31] The phonon lifetime (τ) is directly related to Γ as $\tau = 1/(2\pi c \times \Gamma)$. An anomaly in $\omega(T)$ may also be driven by magnetostriction effect, but this typically does not affect τ and thus should not influence the $\Gamma(T)$ curves. The majority of the modes show a clear deviation in $\Gamma(T)$ from the anharmonic model below T_N . This, provides unambiguous confirmation of the occurrence of SPC in this system. Furthermore, the λ values for various modes were estimated from linear fits to the $\Delta\omega$ vs. $\left\{\frac{M(T)}{M_{Max}}\right\}^2$ plots shown in Figs. 7 (c), (d) for the P10 and P22 modes; fits for the other analyzed modes are shown in Fig. S11 in the SM [31]. The obtained λ values range from 0.275 to 1.03 cm⁻¹, which can be compared with values reported for previously studied AFM compounds exhibiting SPC effects, such as MnF₂ ($\lambda = 0.4 \text{ cm}^{-1}$), CuB₂O₄ ($\lambda = 0.02-0.03 \text{ cm}^{-1}$), Ni₂InSbO₆ ($\lambda = 0.55-2.14 \text{ cm}^{-1}$), Ni₂NbBO₆ ($\lambda = -0.33 \text{ cm}^{-1}$), Ni₂NbBO₆ ($\lambda = 0.03 \text{ cm}^{-1}$), Ni₂N to + 0.67 cm⁻¹), $ZnCr_2O_4$ ($\lambda = 3.2-10.0$ cm⁻¹), $CrSiTe_3$ ($\lambda = 0.1-0.2$ cm⁻¹), and 15*R*- BaMnO₃ ($\lambda = 1.2-3.8$ cm⁻¹) 1) [45,56–61]. This suggests that the SPC effect occurring in Ni₂ScSbO₆ is relatively strong. A theoretical estimation of λ for the P10 mode (showing the most prominent deviation) was performed following the simplified lattice model of Sushkov et al. [61]: $\lambda \approx \frac{2\alpha^2 J}{m\omega_0}$, where $\alpha = 2z/3a_B = 6.301\text{Å}^{-1}$ (here, z refers to the nearest-neighbor co-ordination number of Ni, a_B denotes the Bohr radius, J represents the exchange coupling constant, $\omega_0 = 2\left(\frac{K0}{m}\right)^{1/2}$ denotes the frequency of the phonon mode as calculated from the Raman shift, and m is the mass of a Ni atom. Here, J = $3k_{\rm B}\theta_{\rm CW}/zS(S+1)=1.87$ meV, where $\theta_{\rm CW}=-87$ K, $k_{\rm B}$ denotes the Boltzmann constant, and S=1. The calculation results in $\lambda \sim 1.9$ cm⁻¹, which is consistent with the experimentally obtained value of $\lambda \sim 1.03$ cm⁻¹.

G. Synchrotron x-ray diffraction: magnetostriction effect

 $\Delta\omega_{latt}$, arising from changes in ionic binding energy induced by the lattice contraction or expansion, may contribute significantly to the changes in the phonon frequencies [55]. Hence, a comprehensive study of crystal structure evolution across magnetic transition temperatures in SPC systems is essential. We performed high-resolution SXRD measurements from 300 K to 20 K, as shown in Fig. S12(a) and (b) of the SM. No peak splitting and/or drastic changes in peak shapes were observed throughout the studied temperature range, ruling out a structural phase transition down to 20 K. All data were satisfactorily fitted using the same trigonal symmetry structural model (R3). The SXRD data collected at T = 100 K and 20 K, along with their Rietveld refined profiles, are shown in Fig. S13 of the SM [31]. However, integrated peak intensity analysis revealed an anomalous change at T_N for various Bragg peaks, as demonstrated in Fig. S14 of the SM [31]. Further investigations into the thermal variation of the lattice parameters (a = b, c), and the unit cell volume (V) reveal pronounced anomalies at T_N , as evident in Figs. 8

(a), (b), and (c). A dramatic down-turn is observed in a(T) below T_N , indicating an anomalous lattice contraction along the crystallographic a-axis. In contrast, the c(T) curve exhibits a pronounced up-turn below T_N , indicating anomalous thermal expansion along the c-axis. A distinct down-turn in the V(T) curve is also observed below T_N , indicating a sizeable lattice distortion. If the lattice distortion is sufficiently large, quantifying the spontaneous volume magnetostriction effect using this method is advantageous compared to strain gauge and capacitive techniques [62,63]. The thermal expansion law can be applied to the lattice parameters using the following

expressions:
$$a(T) = a_0 \left[1 + \frac{Be^{\frac{d}{T}}}{T\left(e^{\frac{d}{T}}-1\right)^2} \right]; c(T) = c_0 \left[1 + \frac{fe^{\frac{g}{T}}}{T\left(e^{\frac{g}{T}}-1\right)^2} \right]; \text{ and } V(T) = V_0 \left[1 + \frac{A}{\left(e^{\frac{\theta}{T}}-1\right)} \right]; \text{ here } a_0, c_0, \text{ and } v(T) = v_0 \left[1 + \frac{A}{\left(e^{\frac{\theta}{T}}-1\right)^2} \right]; \text{ here } a_0, c_0, \text{ and } v(T) = v_0 \left[1 + \frac{A}{\left(e^{\frac{\theta}{T}}-1\right)^2} \right]; \text{ here } a_0, c_0, \text{ and } v(T) = v_0 \left[1 + \frac{A}{\left(e^{\frac{\theta}{T}}-1\right)^2} \right]; \text{ here } a_0, c_0, \text{ and } v(T) = v_0 \left[1 + \frac{A}{\left(e^{\frac{\theta}{T}}-1\right)^2} \right]; \text{ here } a_0, c_0, \text{ and } v(T) = v_0 \left[1 + \frac{A}{\left(e^{\frac{\theta}{T}}-1\right)^2} \right]; \text{ here } a_0, c_0, \text{ and } v(T) = v_0 \left[1 + \frac{A}{\left(e^{\frac{\theta}{T}}-1\right)^2} \right]; \text{ here } a_0, c_0, \text{ and } v(T) = v_0 \left[1 + \frac{A}{\left(e^{\frac{\theta}{T}}-1\right)^2} \right]; \text{ here } a_0, c_0, \text{ and } v(T) = v_0 \left[1 + \frac{A}{\left(e^{\frac{\theta}{T}}-1\right)^2} \right]; \text{ here } a_0, c_0, \text{ and } v(T) = v_0 \left[1 + \frac{A}{\left(e^{\frac{\theta}{T}}-1\right)^2} \right]; \text{ here } a_0, c_0, \text{ and } v(T) = v_0 \left[1 + \frac{A}{\left(e^{\frac{\theta}{T}}-1\right)^2} \right]; \text{ here } a_0, c_0, \text{ and } v(T) = v_0 \left[1 + \frac{A}{\left(e^{\frac{\theta}{T}}-1\right)^2} \right]; \text{ here } a_0, c_0, \text{ and } v(T) = v_0 \left[1 + \frac{A}{\left(e^{\frac{\theta}{T}}-1\right)^2} \right]; \text{ here } a_0, c_0, \text{ and } v(T) = v_0 \left[1 + \frac{A}{\left(e^{\frac{\theta}{T}}-1\right)^2} \right]; \text{ here } a_0, c_0, \text{ and } v(T) = v_0 \left[1 + \frac{A}{\left(e^{\frac{\theta}{T}}-1\right)^2} \right]; \text{ here } a_0, c_0, \text{ and } v(T) = v_0 \left[1 + \frac{A}{\left(e^{\frac{\theta}{T}}-1\right)^2} \right]; \text{ here } a_0, c_0, \text{ and } v(T) = v_0 \left[1 + \frac{A}{\left(e^{\frac{\theta}{T}}-1\right)^2} \right]; \text{ here } a_0, c_0, \text{ and } v(T) = v_0 \left[1 + \frac{A}{\left(e^{\frac{\theta}{T}}-1\right)^2} \right]; \text{ here } a_0, c_0, \text{ and } v(T) = v_0 \left[1 + \frac{A}{\left(e^{\frac{\theta}{T}}-1\right)^2} \right]; \text{ here } a_0, c_0, \text{ and } v(T) = v_0 \left[1 + \frac{A}{\left(e^{\frac{\theta}{T}}-1\right)^2} \right]; \text{ here } a_0, c_0, \text{ and } v(T) = v_0 \left[1 + \frac{A}{\left(e^{\frac{\theta}{T}}-1\right)^2} \right]; \text{ here } a_0, c_0, \text{ and } v(T) = v_0 \left[1 + \frac{A}{\left(e^{\frac{\theta}{T}}-1\right)^2} \right]; \text{ here } a_0, c_0, \text{ and } v(T) = v_0 \left[1 + \frac{A}{\left(e^{\frac{\theta}{T}}-1\right)^2} \right]$$

 V_0 denote the lattice constants at T=0 K, whereas B,d,f,g, and A denote adjustable parameters. θ_D refers to the Debye temperature [14]. While the T-dependence of the lattice parameters closely follows the expected thermal expansion behavior above T_N , a pronounced deviation is observed below T_N , as illustrated in Figs. 8 (a)-(c). This deviation suggests an isostructural distortion resulting from a magnetostriction effect, which is induced by the onset of complex AFM spin ordering below T_N . The various fitting parameters thus obtained are summarized in Table SIII of the SM [31]. The spontaneous volume magnetostriction (λ_{ms}^V) at a specific temperature can be estimated by examining the difference in volume between a system in an ordered magnetic state and in the paramagnetic (PM) state [64] as expressed by the formula: $\lambda_{ms}^V(T) = \frac{V_{AFM}(T) - V_{PM}(T)}{V_{PM}(T)}$. Here, $V_{AFM}(T)$ denotes the volume of the system in the AFM state at a temperature T, while $V_{PM}(T)$ refers to the volume the system would have if it were in the PM state at the same temperature. For Ni₂ScSbO₆, the inset of Fig. 8 (c) displays λ_{ms}^V as a function of T, highlighting the significant emergence of the magnetostriction effect below T_N . At T=20 K, λ_{ms}^V is $\sim 3 \times 10^4$, which is comparable to the spontaneous volume magnetostriction values previously reported for 15R- BaMnO₃ ($\lambda_{ms}^V \sim 32 \times 10^4$ at 90 K), Fe₃(PO₄)O₃ ($\lambda_{ms}^V \sim 7.8 \times 10^4$ at 100 K), and Zn_{1-x}Cu_xCr₂Se₄ ($\lambda_{ms}^V \sim 4.6-24.9 \times 10^4$ at 100 K for varying x values) [14,42,64].

In addition to the observed changes in the lattice constants a, c, and V, our analysis suggests that the Ni(1)O₆ and Ni(3)O₆ octahedra showed concomitant changes in their associated bond-lengths and bond-angles below T_N , as demonstrated in Fig. 9 (a) -(f). Additional parameters are shown in Fig. S15 of the SM [31]. The corresponding structural distortion below T_N is schematically illustrated in Fig. 9 (g). Nearest neighbor Ni spins (with a distance \sim 3.78 Å) are coupled via the superexchange pathway Ni(1)-O(1)-Ni(3). Next-nearest neighbor Ni spins (Ni(1)-Ni(1) or Ni(3)-Ni(3) pairs lying in the ab plane at a distance \sim 5.16 Å) are coupled through weaker exchange pathways via ScO₆ and SbO₆ involving both O(1) and O(2). Our SXRD analysis indicates a much larger displacement for O(1)

than for O(2) [as evident from Fig. 9 (g)]. This can presumably be attributed to the predominant exchange interactions via the Ni(1)-O(1)-Ni(3) exchange pathway.

The Grüneisen model connects changes in phonon mode frequency $(\Delta\omega/\omega)$ to changes in unit-cell volume $(\Delta V/V)$ [14]. This relationship is expressed as $(\Delta\omega/\omega) = -\gamma(\Delta V/V)$, where γ is the Grüneisen parameter for a given phonon mode. Plots of $(\Delta\omega/\omega)$ vs. $(\Delta V/V)$ exhibit a linear nature, as illustrated in Figs. 10 (a) and (b) for modes P10 and P22 and Fig. S16 of the SM for other relevant modes. This further emphasizes the crucial role of lattice distortion in inducing anomalous phonon behavior in Ni₂ScSbO₆. Consequently, the present study confirms strong direct spin-phonon coupling, along with lattice distortion driven by the magnetostriction effect that facilitates indirect coupling of spins and phonons. Typically, the contribution of magnetostriction to the SPC effect is considered negligible when reporting SPC effects in various systems [65,66]. Thus, the present study may provide new insights into the SPC effect, particularly in systems with complex magnetic ordering.

IV. CONCLUSION

In conclusion, our comprehensive study highlights the intriguing material Ni₂ScSbO₆, which exhibits a range of exotic phenomena that are strongly interconnected due to the cross-coupling between spin, dipole, lattice, and phonon degrees of freedom. We observe an incommensurate SDW AFM spin ordering at $T_N = 62$ K, which is robust under magnetic fields of up to 4 T, as revealed by magnetization, specific heat, and neutron diffraction studies. Dielectric investigations reveal a λ -shaped peak in the $\varepsilon'(T)$ curves, whose position remains unchanged with frequency but is significantly suppressed under applied magnetic field, demonstrating pronounced magnetodielectric coupling at T_N . A substantial phonon renormalization, evidenced by the anomalous softening of various Raman modes below T_N , is observed, demonstrating a direct entanglement between spin and phonon degrees of freedom. Moreover, high-resolution SXRD studies quantitatively reveal a significant magnetostriction effect, manifested by an unusual thermal variation in the unit cell volume (V) below T_N . Further analysis using Grüneisen's law shows that the observed anomalous phonon softening is significantly influenced by the magnetostriction effect, in addition to the direct spin-phonon coupling (SPC) effect. The strong correlations among these phenomena may provide valuable insight into the coupling phenomena of various microscopic degrees of freedom in other complex magnetic systems.

ACKNOWLEDGMENTS

SC is thankful to CIFC, IIT (BHU) Varanasi, for providing access to the magnetometer (MPMS) facility. HDY acknowledges the generous support from the National Science and Technology Council of Taiwan through the grants: NSTC-113-2112-M110-006 and NSTC-113-2112-M110-022. A.P. gratefully acknowledges the support received from the European Commission through the Horizon Europe MSCA Postdoctoral Fellowship, project number 101110742. We also express our sincere gratitude to the Australian Nuclear Science and Technology Organization (ANSTO) for granting essential access to their experimental facilities.

Table I: Neutron powder diffraction (NPD) fit parameters for different models of magnetic ordering.

Model	χ^2	Magnetic R-factor	$M\left(\mu_{\mathrm{B}}\right)$	
Model_1: SDW	13.1	5.870	2.7261	
Model_2: Spins in ac plane	13.5	7.550	2.6488	
Model_3: Spins in bc plane	13.8	7.527	2.6672	
Model_4: Spins in <i>ab</i> plane	20.2	22.49	1.6108	

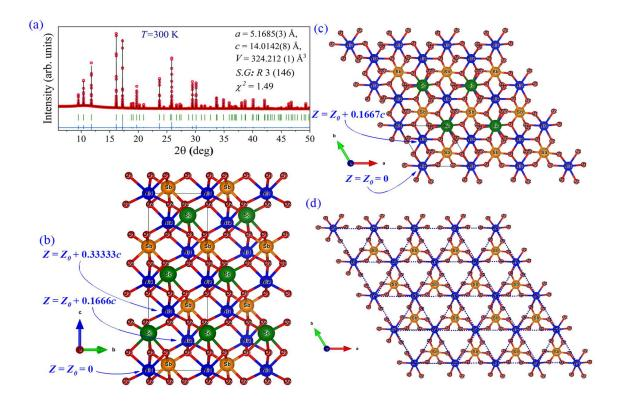


Fig. 1. (a) XRD pattern of Ni₂ScSbO₆ at 300 K (red data points) fitted by Rietveld refinement (black line). The difference profile is shown in blue. (b) Representation of the three-dimensional crystal structure. (c) and (d) Views of the crystal structure in two different *ab* planes, on which the Ni atoms form triangular networks. The blue dashed lines serve as a guide to the eye.

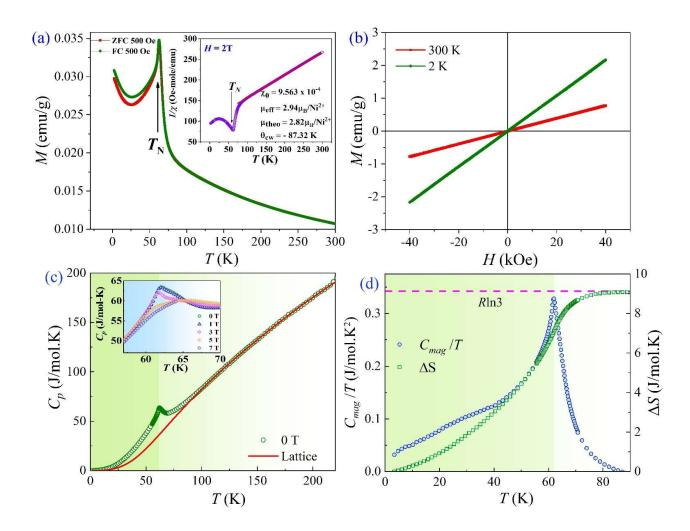


Fig. 2. (a) T-dependence of ZFC and FC magnetic susceptibility recorded under H = 500 Oe. Inset: Curie-Weiss fit of $1/\chi vs$. T curve (recorded under H = 20 kOe) in the paramagnetic regime. (b) Isothermal magnetization versus applied field curves measured at T = 2 and 300 K. (c) Temperature-dependent zero-field specific heat (C_p) curve along with its Debye function fit (shown in red). Inset: $C_p(T)$ curves recorded under various H. (d) C_{mag}/Tvs . T curve at H = 0 T and the corresponding magnetic entropy (ΔS) variation as a function of temperature. Here, C_{mag} denotes the magnetic specific heat.

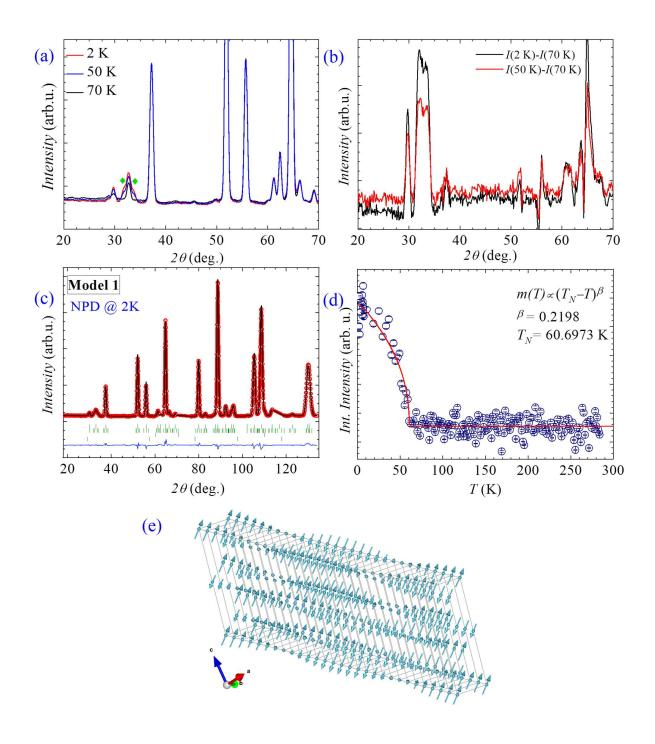


Fig. 3. (a) Neutron diffraction patterns at 2 K, 50 K, and 70 K. The peaks marked by green diamond symbols indicate purely magnetic peaks that appear only below T_N . (b) Neutron diffraction patterns at 2 K and 50 K with the 70 K data subtracted to show the magnetic Bragg peaks and (c) Observed (red data points), fitted (black line) and difference (blue line) neutron diffraction profiles at 2 K. The green vertical bars represent (top to bottom) Bragg reflection positions for Ni₂ScSbO₆ (nuclear and magnetic) and NiO (nuclear and magnetic) impurity, respectively. (d) Power law fit to the temperature dependence of the integrated intensity of the (003) Bragg reflection. (e) A pictorial representation of the SDW spin ordering of Ni₂ScSbO₆ as obtained from the analysis of the NPD data at 2 K.

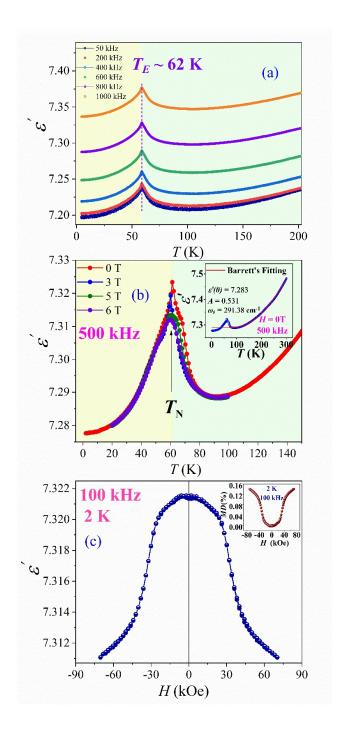


Fig. 4. (a) Temperature-dependence of dielectric constant (ε') at various frequencies. (b) $\varepsilon'(T)$ curves measured under various magnetic fields. Inset: Barrett's fit to $\varepsilon'(T)$ curve measured with a frequency of 500 kHz and under H=0 T. (c) Isothermal magnetic field variation of ε' at 2 K and f=100 kHz. Inset: Field variation of magnetodielectric coupling parameter (MD%).

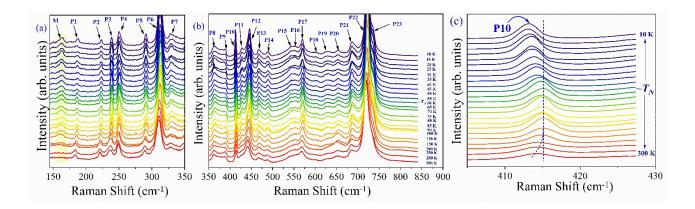


Fig. 5. (a) and (b) Raman spectra in two different frequency regions, collected at various temperatures. Corresponding phonon modes are designated as *P*1 to *P*23. The mode M appears only at lower temperatures, and is denoted as a possible magnon mode. (c) Demonstrates the anomalous softening of the mode P10. The blue dashed lines are the guides to the eye.

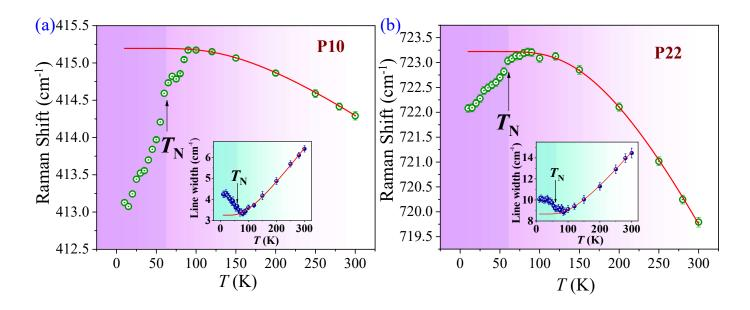


Fig. 6 (a) and (b) Temperature dependence of P10 and P22 phonon mode frequencies, with experimental data (green circles) fitted using an anharmonic law (red solid curve). Insets display the corresponding FWHM dependence on temperature.

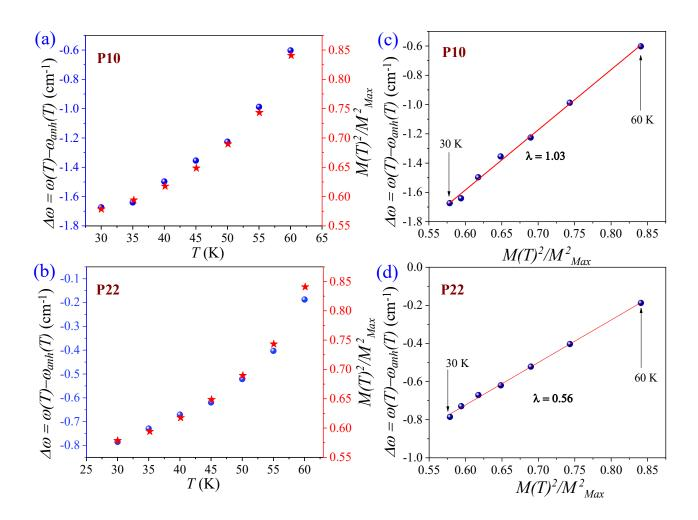


Fig. 7. (a) and (b) Temperature dependence of $\Delta\omega$ and $\{M(T)/M_{Max}\}^2$ for the P10 and P22 modes, respectively. (c) and (d) $\Delta\omega$ vs. $\{M(T)/M_{Max}\}^2$ plots for P10 and P22, with linear fits shown by the red lines.

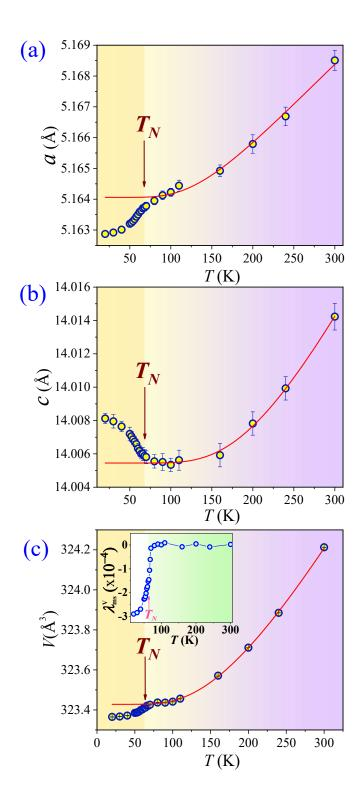


Fig. 8. (a), (b) and (c) Temperature dependence of lattice parameters a, c, and unit-cell volume (V), along with fits to thermal expansion model (red line) in the paramagnetic region. The inset of (c) shows the volume magnetostriction coefficient as a function of temperature.

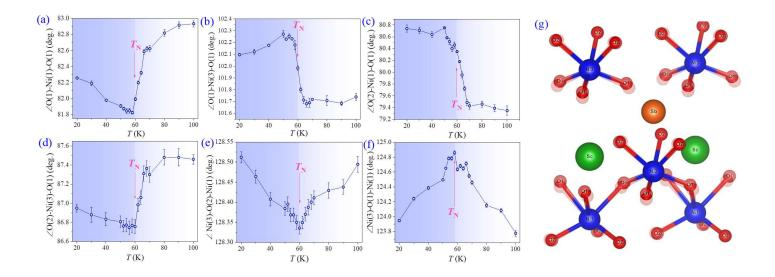


Fig. 9 (a)-(f) Temperature dependence of various bond-angles related to Ni(1)O₆ and Ni(3)O₆ octahedra. T_N , (g) Depiction of change in octahedral structure due to magnetostriction, where the shadowed and solid red spheres represent the positions of oxygen atoms above and below T_N .

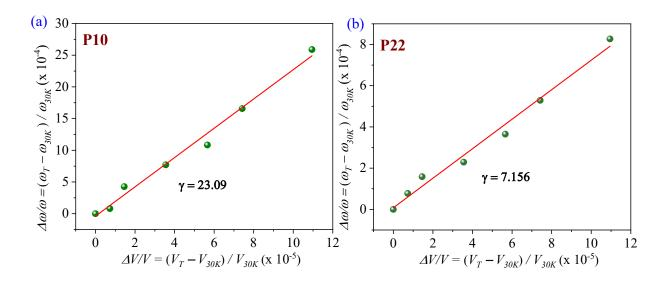


Fig. 10. (a) and (b) $(\Delta\omega/\omega)$ vs. $(\Delta V/V)$ curves for P10 and P22 modes, respectively. The Grüneisen parameter, γ , derived from linear fits (shown in red), indicates a strong correlation between the lattice distortion and phonons.

References

- [1] T. Kim, C. H. Kim, J. Jeong, P. Park, K. Park, K. H. Lee, J. C. Leiner, D. Ishikawa, A. Q. R. Baron, Z. Hiroi, and J.-G. Park, "Spin-orbit coupling effects on spin-phonon coupling in Cd₂Os₂O₇," *Phys. Rev. B*, **102**, 201101 (2020).
- [2] S. Shimomura, K. Tajima, N. Wakabayashi, S. Kobayashi, H. Kuwahara, and Y. Tokura, "Effect of Magnetic Transitions and Charge-Ordering on Crystal Lattice in Nd_{0.5}Sr_{0.5}MnO₃, " *J Physical Soc Japan* **68**, 1943 (1999).
- [3] T. A. Kaplan and S. D. Mahanti, "Canted-spin-caused electric dipoles: A local symmetry theory," *Phys. Rev. B*, **83**, 174432 (2011).
- [4] S. Baidya and T. Saha-Dasgupta, "Electronic structure and phonons in La₂CoMnO₆: A ferromagnetic insulator driven by Coulomb-assisted spin-orbit coupling," *Phys. Rev. B*, **84**, 1 (2011).
- [5] P. Zhao, Z. Zhao, D. Hunter, R. Suchoski, C. Gao, S. Mathews, M. Wuttig, and I. Takeuchi, "Fabrication and characterization of all-thin-film magnetoelectric sensors," *Appl. Phys. Lett.*, **94**, 243507 (2009).
- [6] C. E. Ciomaga, O. G. Avadanei, I. Dumitru, M. Airimioaei, S. Tascu, F. Tufescu, and L. Mitoseriu, "Engineering magnetoelectric composites towards application as tunable microwave filters," *J. Phys. D: Appl. Phys.*, **49**, (2016).
- [7] K. Malleron, A. Gensbittel, H. Talleb, and Z. Ren, "Experimental study of magnetoelectric transducers for power supply of small biomedical devices," *Microelectron. J.*, **88**, 184 (2019).
- [8] S. Chikara, J. Gu, X. G. Zhang, H. P. Cheng, N. Smythe, J. Singleton, B. Scott, E. Krenkel, J. Eckert, and V.
 S. Zapf, "Magnetoelectric behavior via a spin state transition," *Nat. Commun.*, 10, (2019).
- [9] I. Kézsmárki, U. Nagel, S. Bordács, R. S. Fishman, J. H. Lee, H. T. Yi, S.-W. Cheong, and T. Rõõm, "Optical diode effect at spin-wave excitations of the room-temperature multiferroic BiFeO₃," *Phys. Rev. Lett.*, **115**, 127203 (2015).
- [10] R. Nigam, A. V. Pan, and S. X. Dou, "Coexistence of ferromagnetism and cluster glass state in superconducting ferromagnet RuSr₂Eu_{1.5}Ce_{0.5}Cu₂O_{10-δ}," *J. Appl. Phys.*, **105**, 07E303 (2009).
- [11] M. Hase, I. Terasaki, and K. Uchinokura, "Observation of the spin-Peierls transition in linear Cu²⁺ (spin-1/2) chains in an inorganic compound CuGeO₃," *Phys. Rev. Lett.*, **70**, 3651 (1993).
- [12] Y. S. Tang, J. H. Zhang, L. Lin, R. Chen, J. F. Wang, S. H. Zheng, C. Li, Y. Y. Zhang, G. Z. Zhou, L. Huang, Z. B. Yan, X. M. Lu, D. Wu, X. K. Huang, X. P. Jiang, and J.-M. Liu, "Metamagnetic transitions and magnetoelectricity in the spin-1 honeycomb antiferromagnet Ni₂Mo₃O₈," *Phys. Rev. B*, 103, 014112 (2021).
- [13] A. Pal, K. Anand, T. W. Yen, A. Patra, A. Das, S. M. Huang, E. Blundo, A. Polimeni, H. D. Yang, and S. Chatterjee, "Magnetic properties and coupled spin-phonon behavior in quasi-one-dimensional screw-chain compound BaMn₂V₂O₈," *Phys. Rev. Mater.*, 7, 014402 (2023).

- [14] A. Pal, C. H. Huang, T. W. Yen, P. H. Lee, Y. H. Chang, C. H. Yeh, T. W. Kuo, A. Tiwari, D. C. Kakarla, S. M. Huang, M. C. Chou, H. S. Kunwar, S. Rana, V. G. Sathe, B. H. Chen, Y. C. Chuang, and H. D. Yang, "Spin-induced strongly correlated magnetodielectricity, magnetostriction effect, and spin-phonon coupling in helical magnet Fe₃(PO₄)O₃," *Phys. Rev. B*, 106, 094404 (2022).
- [15] R. L. Rodríguez-Suárez and S. M. Rezende, "Dominance of the phonon drag mechanism in the spin Seebeck effect at low temperatures," *Phys. Rev. B*, **108**, 134407 (2023).
- [16] M. Akazawa, M. Shimozawa, S. Kittaka, T. Sakakibara, R. Okuma, Z. Hiroi, H.-Y. Lee, N. Kawashima, J. H. Han, and M. Yamashita, "Thermal Hall effects of spins and phonons in kagome antiferromagnet Cd-Kapellasite," *Phys. Rev. X*, 10, 041059 (2020).
- [17] H. Schmid, "Multi-ferroic magnetoelectrics," Ferroelectrics, 162(1), 317–338 (1994).).
- [18] F. D. M. Haldane, "Nonlinear field theory of large-spin Heisenberg antiferromagnets: Semiclassically quantized solitons of the one-dimensional easy-axis Néel state," *Phys. Rev. Lett.*, **50**, 1153 (1983).
- [19] S. Seki, X. Z. Yu, S. Ishiwata, and Y. Tokura, "Observation of skyrmions in a multiferroic material," *Science*, **336**, 198 (2012).
- [20] I. O. Troyanchuk, D. V. Karpinsky, M. V. Bushinsky, V. A. Khomchenko, G. N. Kakazei, J. P. Araujo, M. Tovar, V. Sikolenko, V. Efimov, and A. L. Kholkin, "Isothermal structural transitions, magnetization, and large piezoelectric response in Bi_{1-x}La_xFeO₃ perovskites," *Phys. Rev. B*, 83, 054109 (2011).
- [21] M. Sahni, S. Mukaherjee, A. Hamid, D. Kumar, S. Chauhan, and N. Kumar, "Structural, optical, magnetic, dielectric, and photocatalytic properties of Sm- and Ni-substituted BiFeO₃ nanoparticles," *J. Mater. Sci.: Mater. Electron.*, **31**, 7798 (2020).
- [22] M. Melnichuk and L. T. Wood, "Direct Kerr electro-optic effect in noncentrosymmetric materials," *Phys. Rev. A*, **82**, 013821 (2010).
- [23] A. Pal, T. W. Yen, T. W. Kuo, C. W. Wang, S. M. Huang, M. C. Chou, Y. C. Lai, Y. C. Chuang, P. Yanda, A. Sundaresan, H. S. Kunwar, V. G. Sathe, A. Tiwari, D. C. Kakarla, and H. D. Yang, "Unconventional multiferroicity induced by structural distortion and magnetostriction effect in the layered spin-1/2 ferrimagnet Bi2Cu₅B₄O₁₄," *Phys. Rev. B*, 107, 184430 (2023).
- [24] Y. H. Chang, A. Pal, P. T. W. Yen, C. W. Wang, S. Giri, G. R. Blake, J. Gainza, M.-J. Hsieh, J.-Y. Lin, C. Y. Huang, Y. J. Chen, T. W. Kuo, A. Tiwari, D. Chandrasekhar Kakarla, and H. D. Yang, "Field-induced transformation of complex spin ordering and magnetodielectric and magnetoelastic coupling in MnGeTeO₆," *Phys. Rev. B*, 110, 064405 (2024).
- [25] M. O. Yokosuk, S. Artyukhin, A. al-Wahish, X. Wang, J. Yang, Z. Li, S.-W. Cheong, D. Vanderbilt, and J. L. Musfeldt, "Tracking the continuous spin-flop transition in Ni₃TeO₆ by infrared spectroscopy," *Phys. Rev. B*, 92, 144305 (2015).
- [26] Y. Araki, T. Sato, Y. Fujima, N. Abe, M. Tokunaga, S. Kimura, D. Morikawa, V. Ukleev, Y. Yamasaki, C. Tabata, H. Nakao, Y. Murakami, H. Sagayama, K. Ohishi, Y. Tokunaga, and T. Arima, "Metamagnetic

- transitions and magnetoelectric responses in the chiral polar helimagnet Ni₂InSbO₆," *Phys. Rev. B*, **102**, 054409 (2020).
- [27] M.-R. Li, E. E. McCabe, P. W. Stephens, M. Croft, L. Collins, S. V. Kalinin, Z. Deng, M. Retuerto, A. Sen Gupta, H. Padmanabhan, V. Gopalan, C. P. Grams, J. Hemberger, F. Orlandi, P. Manuel, W.-M. Li, C.-Q. Jin, D. Walker, and M. Greenblatt, "Magnetostriction-polarization coupling in multiferroic Mn₂MnWO₆," *Nat. Commun.*, 8, 2037 (2017).
- [28] S. Ivanov, P. Nordblad, R. Mathieu, R. Tellgren, E. Politova, and G. André, "Short-range spin order and frustrated magnetism in Mn₂InSbO₆ and Mn₂ScSbO₆, " *Eur. J. Inorg. Chem.*, **2011**, 4691 (2011).
- [29] K. Ji, E. Solana-Madruga, M. A. Patino, Y. Shimakawa, and J. P. Attfield, "A new cation-ordered structure type with multiple thermal redistributions in Co₂InSbO₆," *Angew. Chem. Int. Ed.*, **61**, (2022).
- [30] S. A. Ivanov, R. Mathieu, P. Nordblad, R. Tellgren, C. Ritter, E. Politova, G. Kaleva, A. Mosunov, S. Stefanovich, and M. Weil, "Spin and dipole ordering in Ni₂InSbO₆ and Ni₂ScSbO₆ with corundum-related structure," *Chem. Mater.*, **25**, 935 (2013).
- [31] N. Patel, A. Pal, C. W. Wang, G. R. Blake, J. Khatua, S. Arokiasamy, H. S. Kunwar, Y. C. Lai, Y. C. Chuang, V. Sathe, K.-Y. Choi, H. D. Yang, and S. Chatterjee, "Highly entangled magnetodielectric and magnetostriction effects, and spin-phonon coupling in the antiferromagnetic Ni₂ScSbO₆," *Supplementary Material*.
- [32] M. K. Singh, A. K. Bera, A. Kumar, S. M. Yusuf, and R. S. Dhaka, "Antiferromagnetic ordering and glassy nature in the sodium superionic conductor NaFe₂PO₄(SO₄)₂," *Phys. Rev. B*, **109**, (2024).
- [33] S. Pakhira, C. Mazumdar, R. Ranganathan, S. Giri, and M. Avdeev, "Large magnetic cooling power involving frustrated antiferromagnetic spin-glass state in R₂NiSi₃(R=Gd,Er)," *Phys. Rev. B*, **94**, 1 (2016).
- [34] A. Pal, T. W. Kuo, C.-H. Hsu, D. C. Kakarla, A. Tiwari, M. C. Chou, A. Patra, P. Yanda, E. Blundo, A. Polimeni, A. Sundaresan, F. C. Chuang, and H. D. Yang, "Interplay of lattice, spin, and dipolar properties in CoTeMoO₆: Emergence of Griffiths-like phase, metamagnetic transition, and magnetodielectric effect," *Phys. Rev. B*, **105**, 024420 (2022).
- [35] J. Khatua, M. Pregelj, A. Elghandour, Z. Jagličić, R. Klingeler, A. Zorko, and P. Khuntia, "Magnetic properties of the triangular-lattice antiferromagnets Ba₃RB₉O₁₈ (R=Yb, Er)," *Phys. Rev. B*, **106**, (2022).
- [36] T. Okuda, Y. Beppu, Y. Fujii, T. Onoe, N. Terada, and S. Miyasaka, "Specific heat of delafossite oxide CuCr_{1-x}Mg_xO₂ (0≤x≤0.03), "*Phys. Rev. B*, 77, (2008).
- [37] K. Ghosh, C. Mazumdar, R. Ranganathan, S. Mukherjee, and M. De Raychaudhury, "Structural correlation with the Griffiths phase in disordered magnetic systems," *Phys. Rev. B*, **98**, 184419 (2018).
- [38] A. Jain, D. T. Adroja, S. Rayaprol, A. D. Hillier, W. Kockelmann, S. M. Yusuf, and E. V. Sampathkumaran, "Magnetic ground state and excitations in the mixed 3d-4d quasi-one-dimensional spin-chain oxide Sr₃NiRhO₆," *Phys. Rev. B*, **110**, 224415 (2024).

- [39] S. A. Ivanov, R. Mathieu, P. Nordblad, R. Tellgren, C. Ritter, E. Politova, G. Kaleva, A. Mosunov, S. Stefanovich, and M. Weil, "Spin and dipole ordering in Ni₂InSbO₆ and Ni₂ScSbO₆ with corundum-related structure," *Chemistry of Materials*, **25**, 935 (2013).
- [40] Y. Araki, T. Sato, Y. Fujima, N. Abe, M. Tokunaga, S. Kimura, D. Morikawa, V. Ukleev, Y. Yamasaki, *et. al.*, "Metamagnetic transitions and magnetoelectric responses in the chiral polar helimagnet Ni₂InSbO₆," *Phys. Rev. B*, **102**, 054409 (2020).
- [41] M. Mostovoy, "Ferroelectricity in spiral magnets," Phys. Rev. Lett., 96, 067601 (2006).
- [42] B. Poojitha, A. Rathore, A. Kumar, and S. Saha, "Signatures of magnetostriction and spin-phonon coupling in magnetoelectric hexagonal 15R-BaMnO₃," *Phys. Rev. B*, **102**, 134436 (2020).
- [43] P. T. Barton, M. C. Kemei, M. W. Gaultois, S. L. Moffitt, L. E. Darago, R. Seshadri, M. R. Suchomel, and B. C. Melot, "Structural distortion below the Néel temperature in spinel GeCo₂O₄," *Phys. Rev. B*, **90**, 064105 (2014).
- [44] A. Nonato, B. S. Araujo, A. P. Ayala, A. P. Maciel, S. Yanez-Vilar, M. Sanchez-Andujar, M. A. Senaris-Rodriguez, and C. W. A. Paschoal, "Spin-phonon and magnetostriction phenomena in CaMn₇O₁₂ helimagnet probed by Raman spectroscopy," *Appl. Phys. Lett.*, **105**, 222902 (2014).
- [45] M. A. Prosnikov, A. N. Smirnov, V. Yu. Davydov, Y. Araki, T. Arima, and R. V. Pisarev, "Lattice and magnetic dynamics in the polar, chiral, and incommensurate antiferromagnet Ni₂InSbO₆," *Phys. Rev. B*, **100**, 144417 (2019).
- [46] J. H. Lee, D. Wulferding, J. Kim, D. Song, S. R. Park, and C. Kim, "Linear scaling relationship of Néel temperature and dominant magnons in pyrochlore ruthenates," *Phys. Rev. B*, **108**, (2023).
- [47] D. Wulferding, Y. Choi, W. Lee, and K.-Y. Choi, "Raman spectroscopic diagnostic of quantum spin liquids," *J. Phys.: Condens. Matter*, **32**, 045603 (2020).
- [48] D. Wulferding, M. Shay, G. Drachuck, R. Ofer, G. Bazalitsky, Z. Salman, P. Lemmens, and A. Keren, "Relation between cuprate superconductivity and magnetism: A Raman study of (CaLa)₁(BaLa)₂Cu₃O_y," *Phys. Rev. B*, **90**, (2014).
- [49] A. McCreary, J. R. Simpson, T. T. Mai, R. D. McMichael, J. E. Douglas, N. Butch, C. Dennis, R. Valdés Aguilar, and A. R. Hight Walker, "Quasi-two-dimensional magnon identification in antiferromagnetic FePS₃ via magneto-Raman spectroscopy," *Phys. Rev. B*, **101**, (2020).
- [50] E. Balcar, "Spin-wave lifetime in antiferromagnets," *Journal de Physique Colloques* **32**, (1971).
- [51] M. Balkanski, R. F. Wallis, and E. Haro, Anharmonic effects in light scattering due to optical phonons in silicon, Phys Rev B **28**, 1928 (1983).
- [52] A. Pal, K. Anand, N. Patel, A. Das, S. Ghosh, P. T.-W. Yen, S.-M. Huang, R. K. Singh, H. D. Yang, A. K. Ghosh, and S. Chatterjee, "Interplay of spin, phonon, and lattice degrees in a hole-doped double perovskite: Observation of spin–phonon coupling and magnetostriction effect," *J. Appl. Phys.*, **132**, 223906 (2022).

- [53] A. Milosavljević, A. Šolajić, J. Pešić, Y. Liu, C. Petrovic, N. Lazarević, and Z. V. Popović, "Evidence of spin-phonon coupling in CrSiTe₃," *Phys. Rev. B*, **98**, 1 (2018).
- [54] R. Valdés Aguilar, A. B. Sushkov, Y. J. Choi, S.-W. Cheong, and H. D. Drew, "Spin-phonon coupling in frustrated magnet CdCr₂O₄," *Phys. Rev. B*, 77, 024402 (2008).
- [55] E. Granado, A. García, J. A. Sanjurjo, C. Rettori, I. Torriani, F. Prado, R. D. Sánchez, A. Caneiro, and S. B. Oseroff, "Magnetic ordering effects in the Raman spectra of La_{1-x}Mn_{1-x}O₃," *Phys. Rev. B*, **60**, 11879 (1999).
- [56] M. A. Prosnikov, A. N. Smirnov, V. Y. Davydov, R. V. Pisarev, N. A. Lyubochko, and S. N. Barilo, "Magnetic dynamics and spin-phonon coupling in the antiferromagnet Ni₂NbBO₆," *Phys. Rev. B*, **98**, (2018).
- [57] L. D. Casto, A. J. Clune, M. O. Yokosuk, J. L. Musfeldt, T. J. Williams, H. L. Zhuang, M.-W. Lin, K. Xiao, R. G. Hennig, B. C. Sales, J.-Q. Yan, and D. Mandrus, "Strong spin-lattice coupling in CrSiTe₃," *APL Mater.*, 3, 041515 (2015).
- [58] D. J. Lockwood and M. G. Cottam, "The spin-phonon interaction in FeF₂ and MnF₂ studied by Raman spectroscopy," *J. Appl. Phys.*, **64**, 5876 (1988).
- [59] R. D. Mero, C.-H. Lai, C.-H. Du, and H.-L. Liu, "Spectroscopic signature of spin-charge-lattice coupling in CuB₂O₄," *J. Phys. Chem. C*, **125**, 4322 (2021).
- [60] C. Roy and R. C. Budhani, "Raman- and infrared-active phonons in hexagonal BaMnO₃," *Phys. Rev. B*, **58**, 8174 (1998).
- [61] A. B. Sushkov, O. Tchernyshyov, W. Ratcliff, S.-W. Cheong, and H. D. Drew, "Probing spin correlations with phonons in the strongly frustrated magnet ZnCr₂O₄," *Phys. Rev. Lett.*, **94**, (2005).
- [62] X. Ding, Y. S. Chai, F. Balakirev, M. Jaime, H. T. Yi, S.-W. Cheong, Y. Sun, and V. Zapf, "Measurement of the angle dependence of magnetostriction in pulsed magnetic fields using a piezoelectric strain gauge," *Rev. Sci. Instrum.*, **89**, (2018).
- [63] N. B. Ekreem, A. G. Olabi, T. Prescott, A. Rafferty, and M. S. J. Hashmi, "An overview of magnetostriction, its use and methods to measure these properties," *J. Mater. Process. Technol.*, **191**, 96 (2007).
- [64] J. Kusz, S. Juszczyk, and J. Warczewski, "An X-ray diffraction study of magnetostriction in Zn_{1-x}Cu_xCr₂Se₄ (0.2<x<1.0)," *J. Appl. Crystallogr.*, **21**, 898 (1988).
- [65] D. H. Moseley, Z. Liu, A. N. Bone, S. E. Stavretis, S. K. Singh, M. Atanasov, Z. Lu, M. Ozerov, K. Thirunavukkuarasu, Y. Cheng, *et. al*, "Comprehensive studies of magnetic transitions and spin–phonon couplings in the tetrahedral cobalt complex Co(AsPh₃)₂I₂," *Inorg. Chem.*, **61**(43), 17123 (2022).
- [66] V. Goian, E. Langenberg, N. Marcano, V. Bovtun, L. Maurel, M. Kempa, *et. al.*, "Spin-phonon coupling in epitaxial Sr_{0.6}Ba_{0.4}MnO₃ thin films," *Phys. Rev. B*, **95**, 075126 (2017).

Supplementary

Table SI: Refined structural parameters obtained from fitting the SXRD data collected at $300~\mathrm{K},\,100~\mathrm{K}$ and $20~\mathrm{K}.$

Space group *R*3(146)

Parameters	T = 300 K	T = 100 K	T = 20 K
λ (Å)	0.774890	0.619920	0.619920
a (Å)	5.168508(8)	5.164224(13)	5.162872(10)
b (Å)	5.168508(8)	5.164224(13)	5.162872(10)
c (Å)	14.01423(3)	14.00535(4)	14.00812(3)
$V(\mathring{\mathbf{A}}^3)$	324.2129(9)	323.4705(15)	323.3651(12)
α	90.00	90.00	90.00
β	90.00	90.00	90.00
γ	120.00	120.00	120.00
Ni1			
x	0.00000	0.00000	0.00000
\mathbf{y}	0.00000	0.00000	0.00000
z	0.00000	0.00(8)	0.00(8)
Sc			
X	0.00000	0.00000	0.00000
\mathbf{y}	0.00000	0.00000	0.00000
z	0.21000(8)	0.21000(8)	0.21000(8)
Ni3			
X	0.00000	0.00000	0.00000
\mathbf{y}	0.00000	0.00000	0.00000
z	0.50000	0.50000	0.50000
Sb			
X	0.00000	0.00000	0.00000
\mathbf{y}	0.00000	0.00000	0.00000
z	0.70000(8)	0.70000(8)	0.70000(8)
01			
X	0.33670(8)	0.33484(6)	0.32725(6)
\mathbf{y}	0.03800(10)	0.04184(8)	0.03470(10)
z	0.10010(10)	0.09840(10)	0.09964(8)
O2			
x	0.30600(6)	0.31275(6)	0.31506(6)
y	0.35480(8)	0.36200(8)	0.3612(6)
z	0.2713(4)	0.27151(2)	0.27127(2)

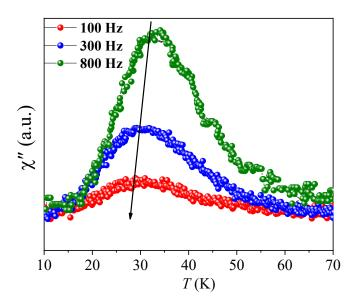


Fig. S1. $\chi''(T)$ (imaginary part of ac susceptibility) curves at different frequencies.

 $\chi''(T)$ curves exhibit a broad peak, which is frequency-dependent. The peak maximum shifts to higher temperatures, and its amplitude increases with increasing frequency, which is a typical feature of the onset of a glassy state. This is in contrast to long-range magnetic order, where no frequency dispersion is observed. Thus, a re-entrant glassy state is observed at temperatures lower than T_N in this system.

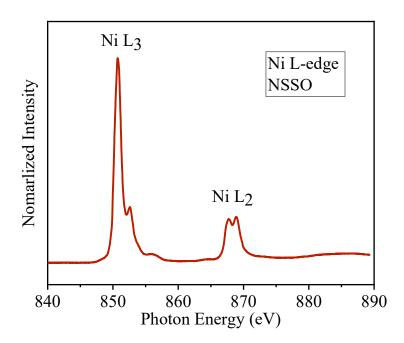


Fig. S2. The X-ray absorption spectrum (XAS) for Ni 2p at the L_2 , L_3 edges, recorded at 300K. The line shape, spin-orbit coupling splitting energy, and the peak positions of the spectrum clearly suggest for the Ni²⁺ oxidation state [1].

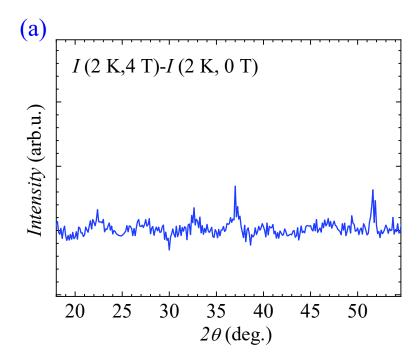


Fig. S3 (a) Difference in 2 K NPD data measured in zero-field compared to 4 T. The diffraction profiles show no significant changes, indicating a stable spin structure under magnetic fields up to 4 T.

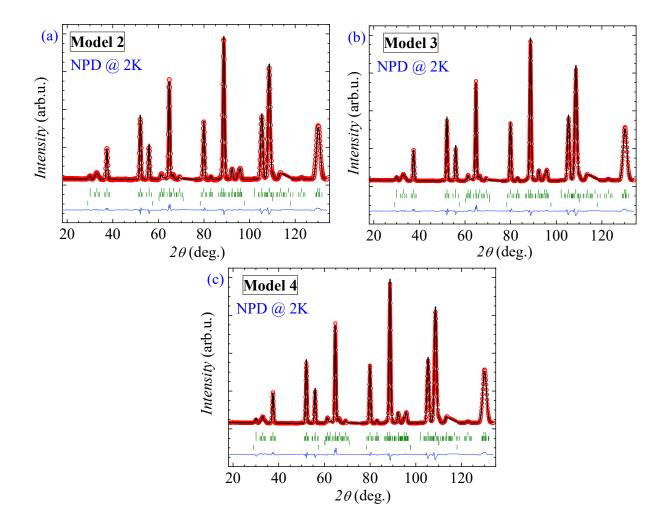


Fig. S4. (a)-(c) Fits (black line) to NPD pattern of Ni₂ScSbO₆ collected at 2 K (red data points) using different models of spin orderings. The blue lines represent the difference profiles. The four top-to-bottom green vertical bars indicate the Bragg reflection positions for Ni₂ScSbO₆ (nuclear and magnetic) and NiO (nuclear and magnetic) impurity, respectively.

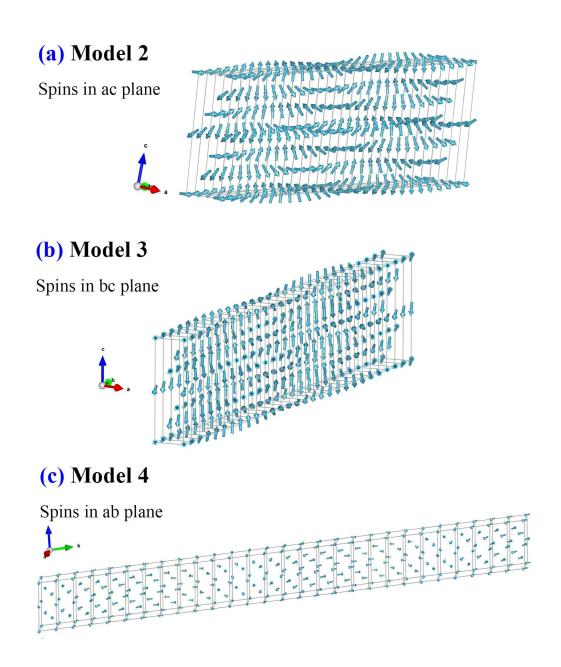


Fig. S5. (a)-(c) Schematic representations of the spin structures derived from various model fittings of the NPD data for Ni2ScSbO6 collected at 2 K.

 $\textbf{Table SII:} \ Comparison \ of the \ Raman \ modes \ reported \ for \ Ni_3TeO_6 \ and \ Ni_2InSbO_6 \ with \ those \ observed \ for \ Ni_2SeSbO_6.$

Ni ₃ TeO ₆ Calculated mode frequency Ref: [2]	Ni ₃ TeO ₆ Observed Raman mode frequencies at 300 K (in cm ⁻¹) Ref: [2]	Symmetry	Ni ₂ InSbO ₆ (TO) (in cm ⁻¹) Ref: [3]	Ni ₂ InSbO ₆ (LO) (in cm ⁻¹) Ref: [3]	Ni₂ScSbO ₆ (This work)
167	155.74	A	155	158	164 M, 184 P1 (F)
205	206.155	A	204	210	223 P2 (F)
209		E	192		238 P3 (W)
217		Е			250 P4 (W)
264		A			
265	269.60	E	271		290 P5 (W)
297	299.97	E	302		312 P6 (S)
343	340.58	E	351		330 P7 (F)
353	354	A	342	389	360 P8(W), 389 P9 (W)
399		A		419	415 P10 (S)
425	419.9229	E	423		427 P11 (W)
426	435.134	A	444		445 P12 (W)
488	506	E	484		470 P13 (W), 488 P14(W)
512	539.466	1	539	563	548 P15 (W),
562	546.437	A E	333	303	552 P16 (W), 570 P17
302	340.437	L			(S)
601	632.51	A	621	662	628 P18 (F), 651 P19 (W)
622	668.87	E	673 (A)	696 (A)	687 P20 (S)
653	699.471	A	702	706	723 P21 (Max), 736 P22 (W)

^{*}Key: M-Magnon mode; Max-Maximum; W-Weak; S-Strong; F-Faint.

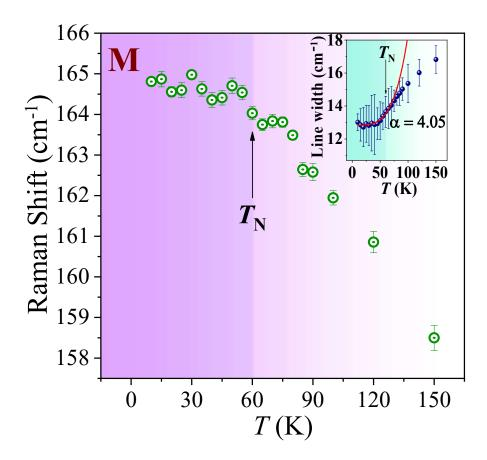


Fig. S6. Temperature variation of the M mode (possible magnon mode) frequency. Inset: corresponding thermal variation of the linewidth of the M mode. The red curve represents a fit using a T^{α} law.

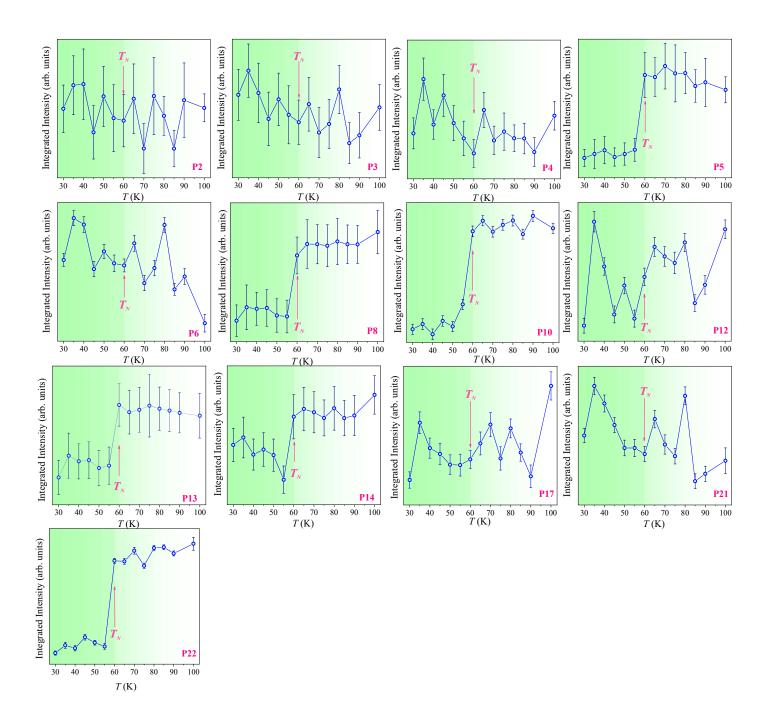


Fig. S7. Temperature dependence of integrated intensities of selected Raman modes.

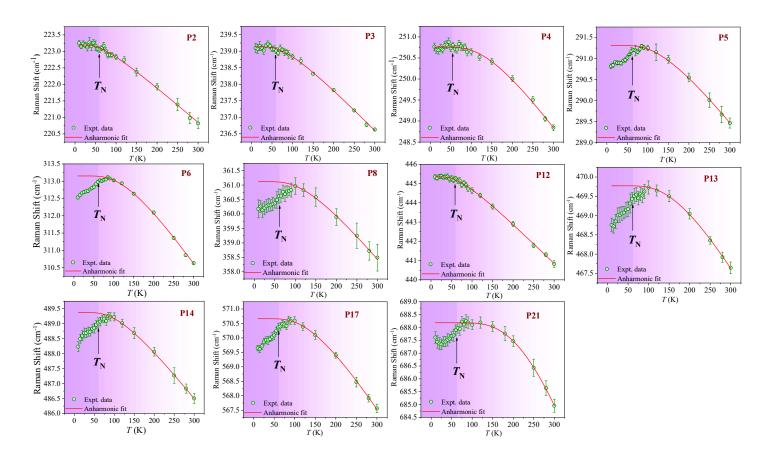


Fig. S8. Temperature dependence of frequencies of selected Raman modes.

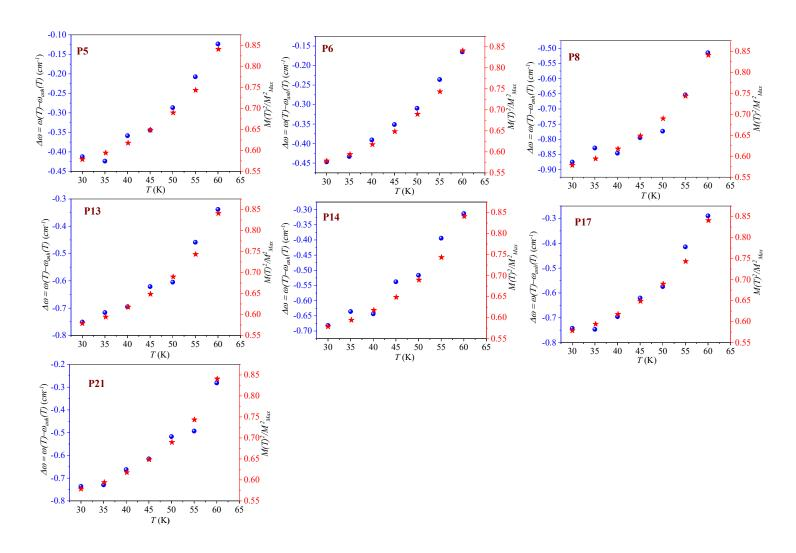


Fig. S9. Temperature dependence of $\Delta \omega$ and $\{M(T)/M_{Max}\}^2$ for selected Raman modes.

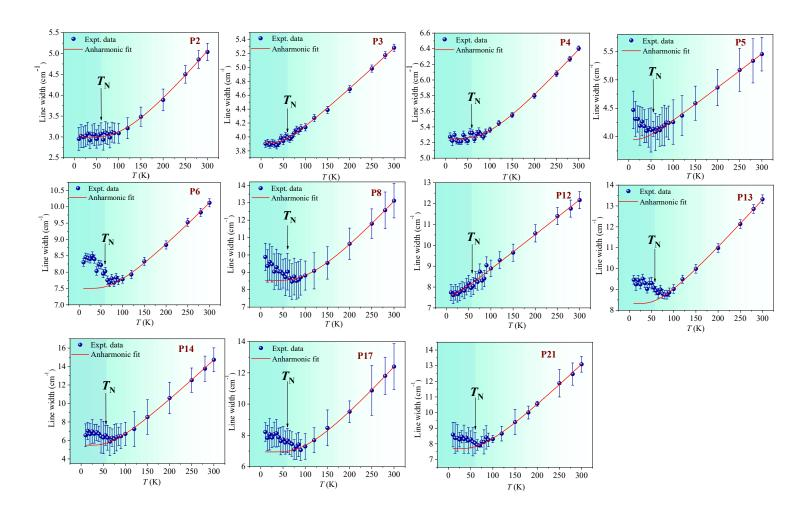


Fig. S10. Temperature dependence of line-widths of selected Raman modes.

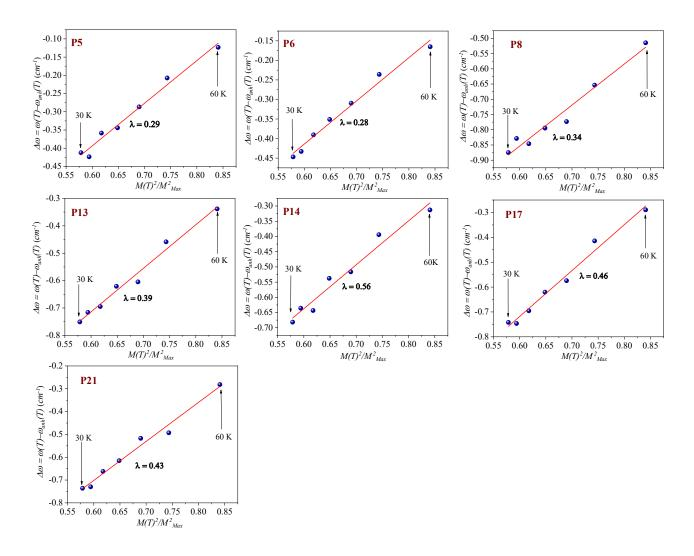


Fig. S11. $\Delta \omega$ vs. $\{M(T) / M_{Max}\}^2$ curves and their linear fits used to determine the SPC constant λ for various modes.

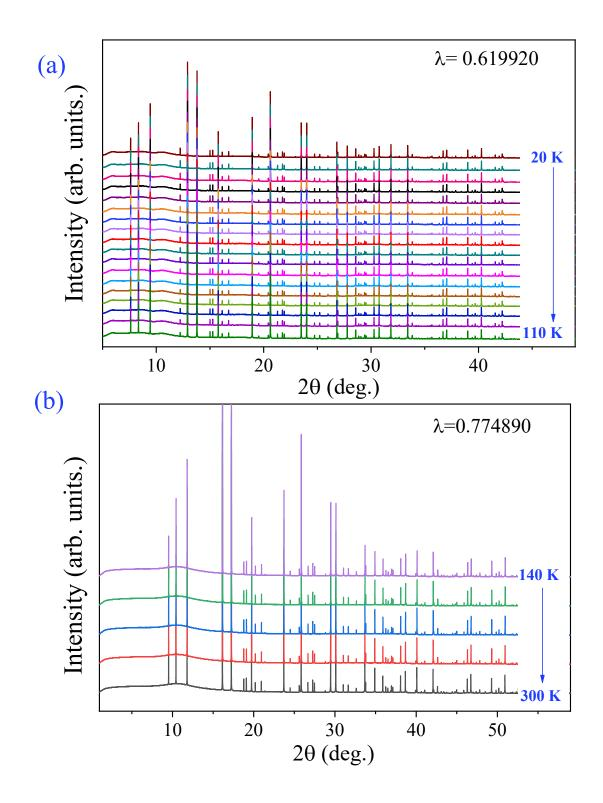
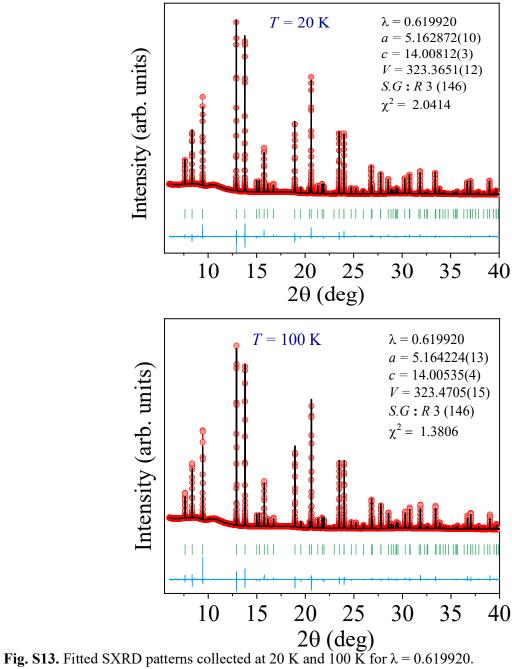


Fig. S12. SXRD patterns (a) collected at temperatures ranging from 20 K to 110 K for $\lambda_i = 0.619920$ and (b) from 140 K to 300 K for $\lambda_i = 0.774890$.



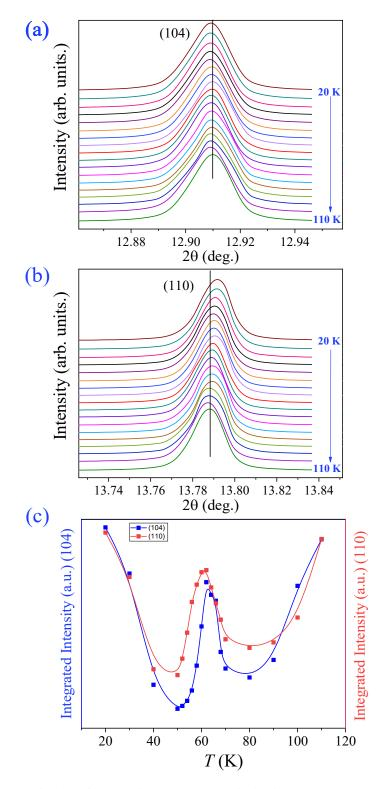


Fig. S14. (a) and (b) Evolution of 104 and 110 SXRD peaks in the temperature range around T_N . (c) Integrated intensity of 104 and 110 SXRD peaks as a function of T.

Table SIII Fitting parameters obtained from the thermal expansion fit to the T dependence of the lattice parameters.

Lattice Parameters	Temperature range (K)	
$a = b (\mathring{A})$	300 K – 60 K	$a_0 = 5.16406(73) \text{ Å}$ B = 1.98(6) and $d = -685(74)$
c (Å)	300 K – 60 K	$c_0 = 14.00545(68) \text{ Å}$ f = 5.7(1) and $g = 1040 (51)$
V (ų)	300 K – 60 K	$V_0 = 323.4285(59) \text{ Å}^3$ A = 0.0123(13) and $\theta_D = 542(25) \text{ K}$

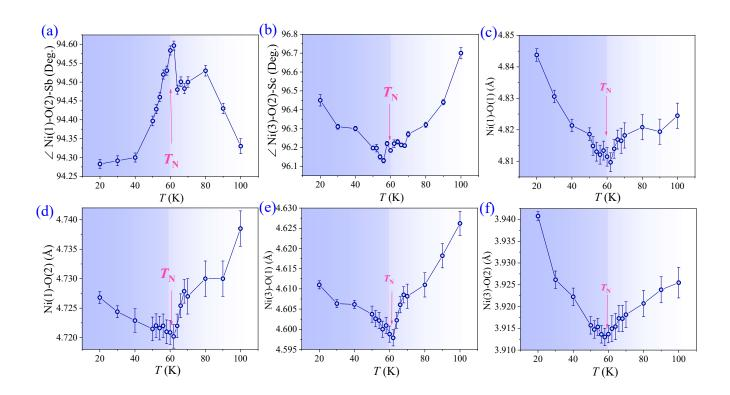


Fig. S15. Temperature dependence of selected bond angles and bond lengths, showing anomalous behavior around T_N .

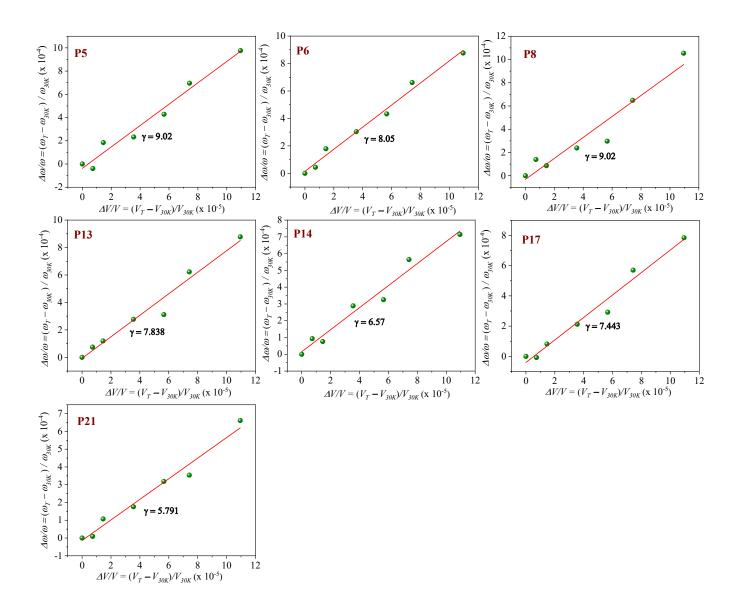


Fig. S16. $(\Delta\omega/\omega)$ vs. $(\Delta V/V)$ curves for various phonon modes. The Grüneisen parameters, γ , are derived from linear fits (red).

References:

- [1] F. Lin, D. Nordlund, T. Pan, I. M. Markus, T. C. Weng, H. L. Xin, and M. M. Doeff, "Influence of synthesis conditions on the surface passivation and electrochemical behavior of layered cathode materials", *J Mater Chem A Mater* 2, 19833 (2014).
- [2] M. O. Yokosuk, S. Artyukhin, A. Al-Wahish, X. Wang, J. Yang, Z. Li, S. W. Cheong, D. Vanderbilt, and J. L. Musfeldt, "Tracking the continuous spin-flop transition in Ni₃TeO₆ by infrared spectroscopy", *Phys Rev B* **92**, 144305 (2015).
- [3] M. A. Prosnikov, A. N. Smirnov, V. Y. Davydov, Y. Araki, T. Arima, and R. V. Pisarev, "Lattice and magnetic dynamics in the polar, chiral, and incommensurate antiferromagnet Ni₂InSbO₆", *Phys Rev B* **100**, (2019).